Materials Chemistry and Physics xxx (xxxx) 125854

Contents lists available at ScienceDirect

Materials Chemistry and Physics

journal homepage: www.elsevier.com/locate/matchemphys

Role of sintering temperature on electronic and mechanical properties of thermoelectric material: A theoretical and experimental study of TiCoSb half-Heusler alloy

Ajay Kumar Verma [a, b], Kishor Kumar Johari [a, b], Kriti Tyagi [a], Durgesh Kumar Sharma [c, 1], Pawan Kumar [c], Sudhir Kumar [c], Sivaiah Bathula [d], S.R. Dhakate [a, b, **], Bhasker Gahtori [a, b, *]

[a] CSIR-National Physical Laboratory, Dr. K.S. Krishnan Marg, New Delhi, 110012, India
[b] Academy of Scientific and Innovative Research (AcSIR), Ghaziabad, 201002, India
[c] Applied Physics Department, Faculty of Engineering and Technology, M. J. P. Rohilkhand University, Bareilly, 243006, India
[d] School of Minerals, Metallurgical and Materials Engineering, IIT Bhubaneswar, 752050, India

ARTICLE INFO

Keywords:
Thermoelectric
Power factor
Half-heusler
Micro-hardness
Fracture toughness

ABSTRACT

Ternary based half-Heusler (HH) alloys are being widely explored for mid temperature range thermoelectric (TE) applications. Here, we have discussed the effect of sintering temperature on electronic, structural and mechanical properties of TiCoSb HH alloy. Four samples of TiCoSb were synthesized employing arc melting followed by spark plasma sintering at different sintering temperatures. Subsequently, the phase purity of all the synthesized samples was confirmed by X-ray diffraction (XRD) analysis. The crystallite size is calculated employing Williamson-Hall method, which increases monotonically with sintering temperature. The morphology coupled with compositional analysis of the samples was studied employing Field Emission Scanning Electron Microscope (FESEM) and Energy Dispersive X-Ray Spectroscopy (EDS), respectively. Further, these samples were characterized for their electronic transport properties. The overall transport properties which are represented by power factor (PF) found to be increasing with sintering temperature. A maximum value of power factor ~0.79 mW/m-K^2 at 625K is achieved for sample sintered at 1423 K. Furthermore, the mechanical properties (micro-hardness and fracture toughness) were found to be increased monotonically with increasing sintering temperature. To understand the underlying physics, the electronic structure and transport properties of the material have been studied by using first principles-based Density Functional Theory (DFT).

1. Introduction

The development of efficient thermoelectric (TE) material is prerequisite for the fabrication of high-performance TE devices. The efficiency of a TE device primarily depends on dimensionless figure-of-merit (ZT) $ZT = \alpha^2\sigma T/\kappa$, where $\alpha^2\sigma$ represents the electronic performance of materials, comprising of Seebeck coefficient (α) and electrical conductivity (σ), and is defined as power factor (PF), κ represents thermal conductivity, and T is absolute temperature. Half-Heusler(HH) alloys are one of the promising materials for TE applications in mid-temperature range owing to their inherent properties such as high Seebeck coefficient, and high mechanical strength along with good thermal stability [1–9]. In the family of ternary HH alloys, MNiSn (M = Ti, Hf, Zr) and MCoSb based materials have received the attention of researchers for the fabrication of TE device. Motivated by the unmatched TE performance of MNiSn based alloys, ZrNiSn has been widely explored and reported to have high TE performance [10–16], on the other hand, the practical applications of MCoSb are limited due to its low TE performance. Thus, there exists enough scope for improvement in TE performance of MCoSb based HH alloys. Further, these materials are also significantly important for TE applications due to their ability to be tuned up into compatible n- and p-type materials, a prerequisite for TE device fabrication. Among the MCoSb based HH alloys, the band gap of TiCoSb is ~1.06 eV [17,18] which is higher than most of other HH alloys [19,20], this attribute high α, and moderate σ, which is manifests in term of good electronic transport properties of the materials.

* Corresponding author. CSIR-National Physical Laboratory, Dr. K.S. Krishnan Marg, New Delhi, 110012, India.
** Corresponding author. CSIR-National Physical Laboratory, Dr. K.S. Krishnan Marg, New Delhi, 110012, India.
E-mail addresses: dhakate@nplindia.org (S.R. Dhakate), bhasker@nplindia.org (B. Gahtori).
[1] Present Address: Theoretical Sciences Unit, Jawaharlal Nehru Centre for Advanced Scientific Research, Jakkur, Bangalore - 560064, India.

https://doi.org/10.1016/j.matchemphys.2022.125854
Received 19 August 2021; Received in revised form 19 January 2022; Accepted 12 February 2022
0254-0584/

TiCoSb HH alloy exhibits a face centered cubic (fcc) structure with space group $F\bar{4}3m$ (no. 216) [21]. TiCoSb intrinsically is an n-type semiconductor that can also be altered into a p-type TE material via appropriate hole doping [22,23]. Zhou et al. have synthesized TiCoSb HH alloy by employing heating in argon atmosphere then consolidation in spark plasma sintering (SPS) at 1123 K and achieved $\alpha \sim$ -280 μV/K along with σ ~5 x 10^3 Sm^{-1} at ~600 K [24]. Further, Sekimoto et al. have realized$\alpha \sim -300$ μV/K and σ ~3 x 10^3Sm^{-1} at ~650 K for TiCoSb HH alloy, processed via the combination of arc melting and SPS at 1373K then post SPS annealing [25]. Wu et al. have reported the $\alpha \sim -250$ μV/K, and σ ~3.5 x 10^3Sm^{-1} at ~650K in TiCoSb sample processed employing arc melting, followed by two steps annealing then consolidated by SPS at 1223 K at 50 MPa [23]. Qie et al. have synthesized pure TiCoSb employing multistep process of arc melting, annealing, and SPS at 1423 K, and realized $\alpha \sim -270$ μV/K and σ ~7 × 10^3Sm^{-1} at ~680K [26]. Zhou et al. have synthesized pristine TiCoSb via the process of heating and quenched in water, then annealing followed by SPS at 1073 K and have shown $\alpha \sim -360$ μV/K and σ ~3 x 10^3 Sm^{-1} at ~600K [27]. In a nutshell, it is observed that most of the synthesis routs involves multiple processing steps. Also, it is apparent that the sintering temperature plays a crucial role for the optimization of electronic transport properties.

The present work is devoted towards understanding the effect of sintering temperature on structural, electronic, and mechanical properties of TiCoSb. The samples were synthesized by arc melting followed by spark plasma sintering (SPS) at different sintering temperatures of 1273 K, 1323 K, 1373 K and 1423 K at fixed pressure of ~50 MPa, and these synthesized samples are referred as S-1, S-2, S-3, and S-4, respectively. The structural analysis of all the synthesized samples was performed using X-ray diffraction and FESEM techniques. Further these samples were characterized for electronic transport properties. It was observed that the power factor follows an increasing trend with sintering temperature, which is majorly contributed by improved Seebeck coefficient. In addition to high TE performance, the mechanical strength is equally important for device fabrication. In view of this, the mechanical properties were measured and a comprehensive data of these properties for all synthesized samples has been provided. In order to understand the electronic structure of pristine TiCoSb, we have carried out DFT based calculations of the electronic band structure and projected density of states (PDOS). Further, for better understanding of the electronic transport properties, we have extended the band structure calculation to obtain the theoretical electronic transport properties employing BoltzTraP code [28].

2. Experimental details

The high purity elements (Ti-granules, Co-piece, and Sb-shots) in the stoichiometric proportion were melted in an arc melting unit (*MAM-1, Edmund Bühler GmbH*), and the obtained ingots were re-melted 3–4 times after flipping to ensure the homogeneity. Further, using mortar and pestle, the arc melted ingots were hand ground to make fine powder which was then consolidated employing spark plasma sintering (SPS, *Dr. Sinter,725*), at different sintering temperatures (1273 K, 1323 K, 1373 K and 1423 K) and a constant pressure of ~50 MPa and the detailed SPS parameters are shown in Table 1.

The X-ray diffraction technique (XRD, *Rigaku Miniflex II*) was utilized to investigate the phase of all synthesized samples. In order to confirm the phase purity, the Rietveld refinement of XRD patterns was performed using FullProf Suite package. To Study the surface morphology, all the samples were characterized using Field Emission Scanning Electron Microscope (FESEM; *Carl-Zeiss Merlin II*) and Energy Dispersive X-Ray Spectroscopy (EDS; *Oxford Instruments*) was employed to understand the elemental composition. The temperature dependent resistivity and Seebeck coefficient were measured by employing the four-probe method (ULVAC, ZEM-3). The room temperature carrier concentration and carrier mobility of all the samples were observed using Hall effect measurement system (HEMS, Nanomagnetics). The densities of all the samples were measured by Archimedes principle-based system (ML204/A01, Mettler Toledo). To measure the micro-hardness, Future Tech equipment (FM-e7) was used along with a square diamond pyramidal indenter (136°), and the indentation load was fixed at 4.9 N with 10 s dwell time for all well-polished samples. To calculate the fracture toughness of samples, the length of the generated cracks due to the indentation was observed via in-built microscope having micrometer scale in the Vickers micro-hardness system. We have repeated the measurement four times and calculated standard deviation.

Table 1
Sample synthesis parameters in pyrometer mode of SPS and no holding is applied in any step for any sample.

Sample	Max. SPS Temperature (K)	Total time of heating cycle (min.)	Applied Max. Pressure (MPa.)	Max. Voltage (Volts)	Max. current (Ampere)	Displacement (mm)
S-1	1273	14	~ 50	3	500	0.7
S-2	1323	16	~ 50	4	450	0.4
S-3	1373	18	~ 50	5	800	1.0
S-4	1423	20	~ 50	5	700	0.4

3. Computational details

The electronic structure and thermoelectric properties of pristine TiCoSb system were studied by first-principles calculations within the framework of DFT. The DFT implemented VASP (Vienna Ab-initio Simulation Package) [29,30] was considered as a calculator. It incorporates PAW (projected augmented wave) scheme for the calculation of pseudo potentials of elements. In the form of exchange and correlation functional, we opted parameterized form of generalized gradient approximation (GGA) [31]. The plane wave basis sets were expanded by supplying kinetic energy cut-off equal to 550 eV and the integration of first Brillouin Zone (BZ) was carried out by using Γ-centered 20x20x20 k-points mesh for the structure optimization and electronic structure calculations while much denser mesh of size 48x48x48 was considered for transport properties calculations. We use Gaussian smearing method with width of 0.05 eV for all set of calculations. It is important to mentioned here that before extracting properties of considered material, we relax atoms as well as lattice vectors for all degree of freedom of the cell by employing conjugate gradient approximation so that to achieve Hellmann-Feynman residual force minimization criteria upto ≤0.001 eV $Å^{-1}$. We fixed very tight energy convergence criteria equal to 10^{-6} eV for all set of calculations. The thermoelectric properties of considered material have been calculated by using BoltzTraP code [28].

4. Results and discussion

Prior to the experimental characterization rendering of TiCoSb samples, we have gathered the theoretical information about the compound employing DFT calculations. In order to validate our observation and unearth the underlying physics, we start calculation from scratch with the aim to provide a comparative data with the available earlier reports and then make a clear comparison between theoretical predictions and measurements. It was earlier reported that TiCoSb have energy band gap of 0.95 eV by considering local density functional [32,33]. However, the value of band gap depends upon several parameters used into calculations like lattice constants, electron exchange correlation functional, etc. Our optimized unit cell of TiCoSb system is displayed in Fig. 1(a). To understand the electronic structure of material, electronic band structure has been calculated as shown in Fig. 1(b), which clears that pristine TiCoSb exhibits indirect band gap of 1.05 eV with the valence band maxima at Γ, while conduction band minima at X point of the Brillouin Zone (BZ) and rendering the material i[illegible]emiconductor. These

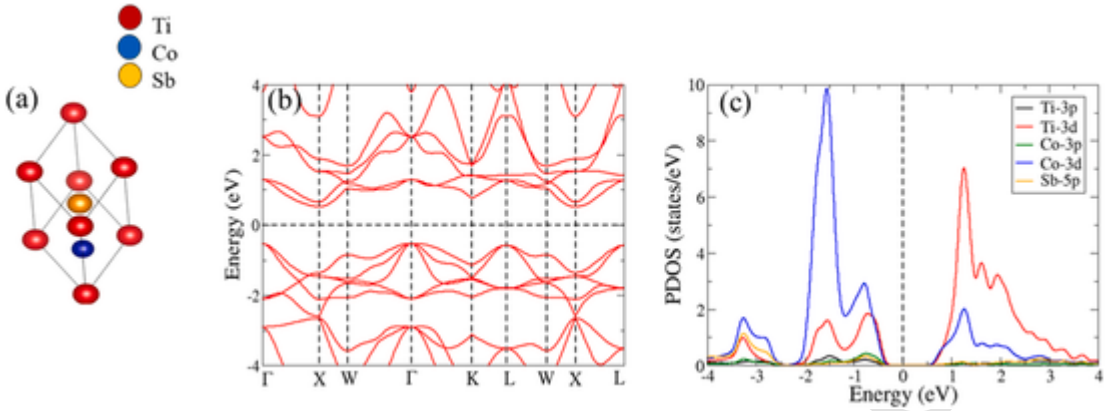

Fig. 1. (a) Optimized unit cell, (b) calculated electronic band structure and (c) projected density of states (PDOS) of TiCoSb system.

features are in good agreement to the predicted by Tobola et al. [32,33] except that the overestimation in band gap predictions which might be due to the use of different correlation function into computations. However, present predictions for energy band gap shows consistency with the earlier reported calculations on pristine TiCoSb [18]. In order to deepen our understanding about the hybridization between atomic orbitals, we additionally performed projected density of states (PDOS) calculations. Looking to the PDOS given in Fig. 1(c), it is apparent that the valence band edge mainly originates due to strong hybridization between Ti-3d and Co-3d states with small contribution of Ti-3p, Co-3p and Sb-5p orbitals. However, the origin of conduction band edge is attributed to Ti-3d and Co-3d states only. These calculations are consistent with the earlier calculated data of total density of states with improved separation between valence and conduction band edges, may be due to used precise correlations between electrons [33].

The X-ray diffraction patterns of all the synthesized TiCoSb samples are illustrated in Fig. 2(a), which exhibit all the peaks are well indexed with single phase of TiCoSb HH (PDF Card No. 00-030-0083). To investigate the phase purity, Rietveld refinement of XRD pattern of all the synthesized samples was performed and the extracted crystallographic parameters along with goodness of fit are shown in Table 2. The refined XRD pattern of all the samples S-1 toS-4 is shown in Fig. 2(b–e). The lattice parameters of all the synthesized samples gotten from Rietveld refinement (shown in Table 2), do not show any appreciable change. Further the density of all the samples has been measured by employing Archimedes principle. The densities of samples are very close to the theoretical density. The relative density of the sample increases monotonically with increasing sintering temperature as shown in Table 2. To observe the effect of sintering temperature on crystallite size and generated lattice strain in the samples, we have used the well-known Williamson-Hall method [34];

$$\beta\, cos\theta = \frac{K\lambda}{D} + 4\varepsilon\, sin\theta$$

Here β is FWHM corresponding to each peak in XRD data in radians, θ is half of diffraction angle, K is shape factor and taken as 0.9, λ is the wavelength of Cu Kα source generated X-rays, D is Crystallite size and ε is the generated lattice strain. The evaluated crystallite size and lattice strain of all the synthesized samples are presented in Fig. 2(f). It is clear from Fig. 2(f) that the crystallite size increases significantly with increasing sintering temperature, because higher sintering temperature provides more intensive atomic diffusion, which is the cause of crystallites growth, and the higher heating rate effectively diminishes the crystallites growth because of the insufficient time for atomic diffusion [35,36]. Therefore, sample S-4 has larger crystallites size compared to others due to the relatively low heating rate along with high sintering temperature. However, the generated lattice strain exhibits marginal change with sintering temperature.

The surface morphology and elemental composition, of the synthesized samples were investigated employing FESEM and EDS. From Fig. 3 it is clear that the significant variation in the grains size was not observed from the FESEM images, but from the FESEM data it was observed that the grains are being more compact as sintering temperature rises which is in accordance with the variation of density with sintering temperature as observed experimentally (Table 2). Moreover FESEM images correspond to each sample exhibits surface homogeneity. EDS analysis confirm that all samples S-1, S-2, S-3 and S-4 are very close to targeted stoichiometry.

The temperature-reliant electronic transport properties of all the synthesized samples are shown in Fig. 4. The behavior of electrical conductivity with temperature for these samples has been shown in Fig. 4 (a). It is clear from Fig. 4(a), that electrical conductivity of all the samples follow an increasing trend with temperature thus exhibiting the semiconducting behavior. Further, at room temperature (RT), σ decreases as sintering temperature increases, i.e. σ of S-1 is higher than that of S-2, S-3 and S-4, and lies in the range (0.78–0.35) x 10^3 Sm^{-1}, which is very close to previous reports [37,38]. To understand the behavior of σ, we performed Hall measurement at RT and obtained the value of carrier concentration (n) and carrier mobility (μ) shown in Table 3 it is clear from Table 3 that the carrier density is observed in decreasing order with increasing sintering temperature which lead to increase in the mobility of the sample with sintering temperature except sample S-3, according to the relation $\mu = \sigma/ne$, which are in same trend as observed in literature [39]. This decreasing behavior of carrier density with sintering temperature is may be due to the reduction in ionized impurities, because usually TiCoSb and other half-Heusler are not obtained in single phase after arc melting and they tend to get single phase in SPS at optimized temperature [40]. This reduction of impurities with increasing sintering temperature is responsible for decrease in scattering of carriers, which may lead to improvement in carrier mobility. The collective effect of carrier concentration and mobility is in well agreement to the observed behavior of σ at RT.

Fig. 4(b) illustrates the temperature-dependent α of all the samples. It is apparent from the figure that all samples exhibit a negative α, which indicates n-type conduction similar to that observed in earlier reports [22,38]. The $|\alpha|$ is increasing with sintering temperature, which may be due to the observed reduction in carrier concentration (Table 3) and increment in effective mass (Fig. 4(d)). In similar manner, Chen et al. have synthesized ZrNiSn based compound at different sintering temperature and realized reduction in carrier concentration which lead to enhancement in $|\alpha|$ with sintering temperature [41]. The similar kind of behavior has also been observed by other groups [39,42,43]. Further, on increasing temperature, α of all TiCoSb samples initially increases up to a certain temperature beyond which α slightly declines, which can be attributed to the effect of bipolar conduction at higher temperature [26]. The highest $|\alpha|$ is observed in sam-

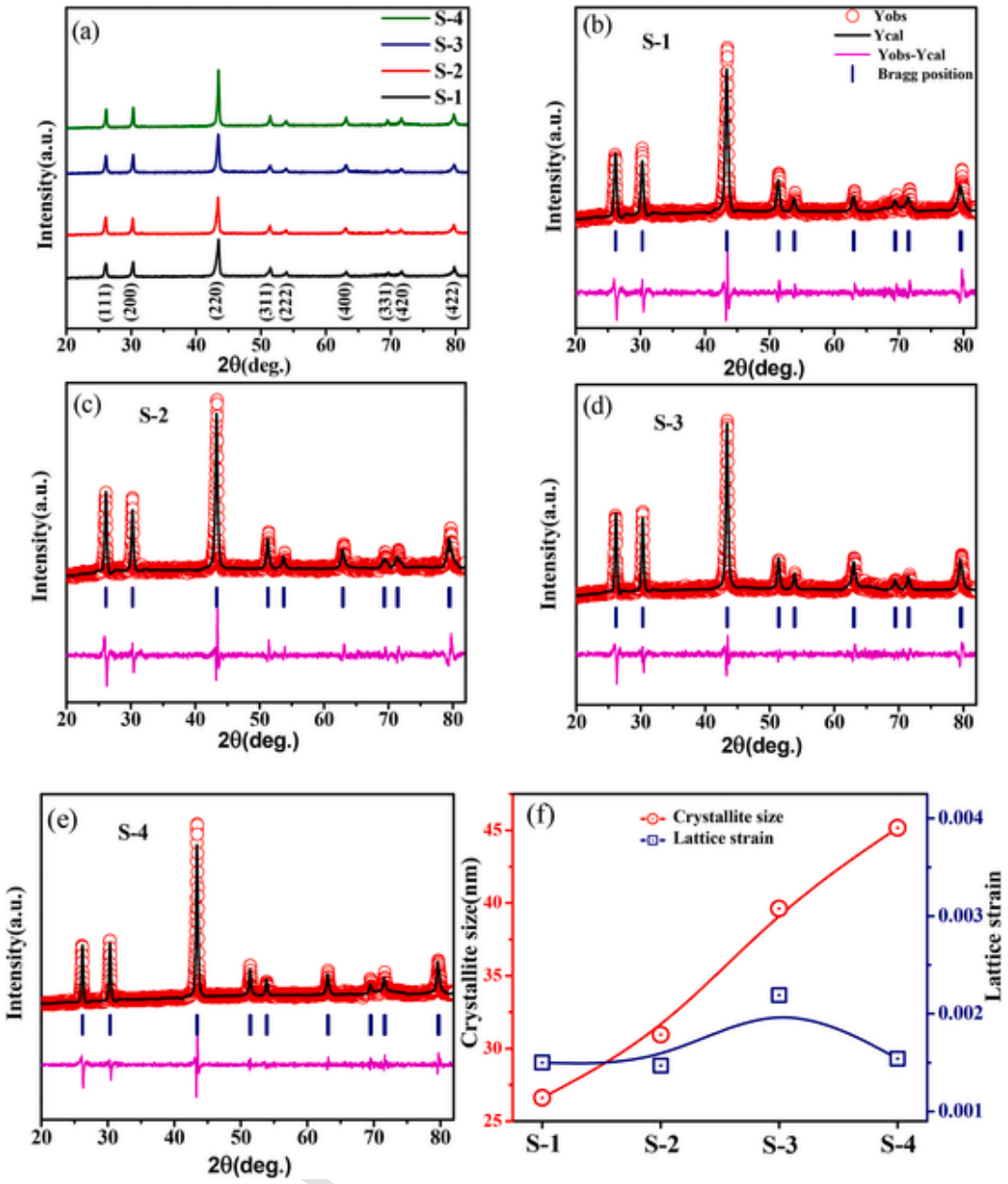

Fig. 2. (a) The XRD patterns of all the samples, (b–e) Rietveld refinement, and (f) Crystallite size along with lattice strain, of all TiCoSb samples.

Table 2
The Rietveld refinement details of all TiCoSb samples along with their relative density.

Sample Details	R_p	R_{wp}	R_e	χ^2	a(Å)	Relative density (%)
S-1	42.6	33.6	17.1	3.868	5.9027	~97.79
S-2	44.4	33.4	17.2	3.782	5.9093	~98.97
S-3	38.4	27.9	17.1	2.674	5.8999	~99.10
S-4	42.9	29.8	16.7	3.181	5.895	~99.19

ple S-4–404 μV/K at 428 K. The collective role of σ and α in the electronic transport, could be observed via power factor (PF), which is defined as ($\alpha^2\sigma$). Fig. 4(c) demonstrates the temperature dependent PF of all the TiCoSb samples in the temperature range from RT to ~873 K. At room temperature, PF increases monotonically with sintering temperature, and lies in the regime from 0.004 to 0.035 mW/m-K^2. The PF of all the synthesized samples initially increases up to a certain operating temperature, beyond that, PF starts to gradually decrease which is the reflection of the combined trend of σ and α. The highest PF (~0.79 mW/mK^2) is realized in the sample S-4 at 625 K. Here it may be noted that in entire temperature regime the PF of S-3 and S-4 are very close to each other. Therefore, it seems appropriate to conclude that the sintering of samples at high temperature is favorable for higher electronic transport properties, and in our findings, ~1373 and 1423 K are the considerable temperatures to achieve elevated electronic transport properties in TiCoSb alloy.

To understand the electronic transport behavior, Seebeck effective mass (m_S^*) was calculated at room temperature using the following equation [44]:

For $|\alpha| > 75$ μV/K

$$m_S^* \approx \frac{h^2}{2k_BT}\left\{\frac{3n}{16\sqrt{\pi}}\left[exp\left(\frac{|\alpha|}{k_B/e}-2\right)-0.17\right]\right\}^{\frac{2}{3}}$$

And for $|\alpha| < 75$ μV/K

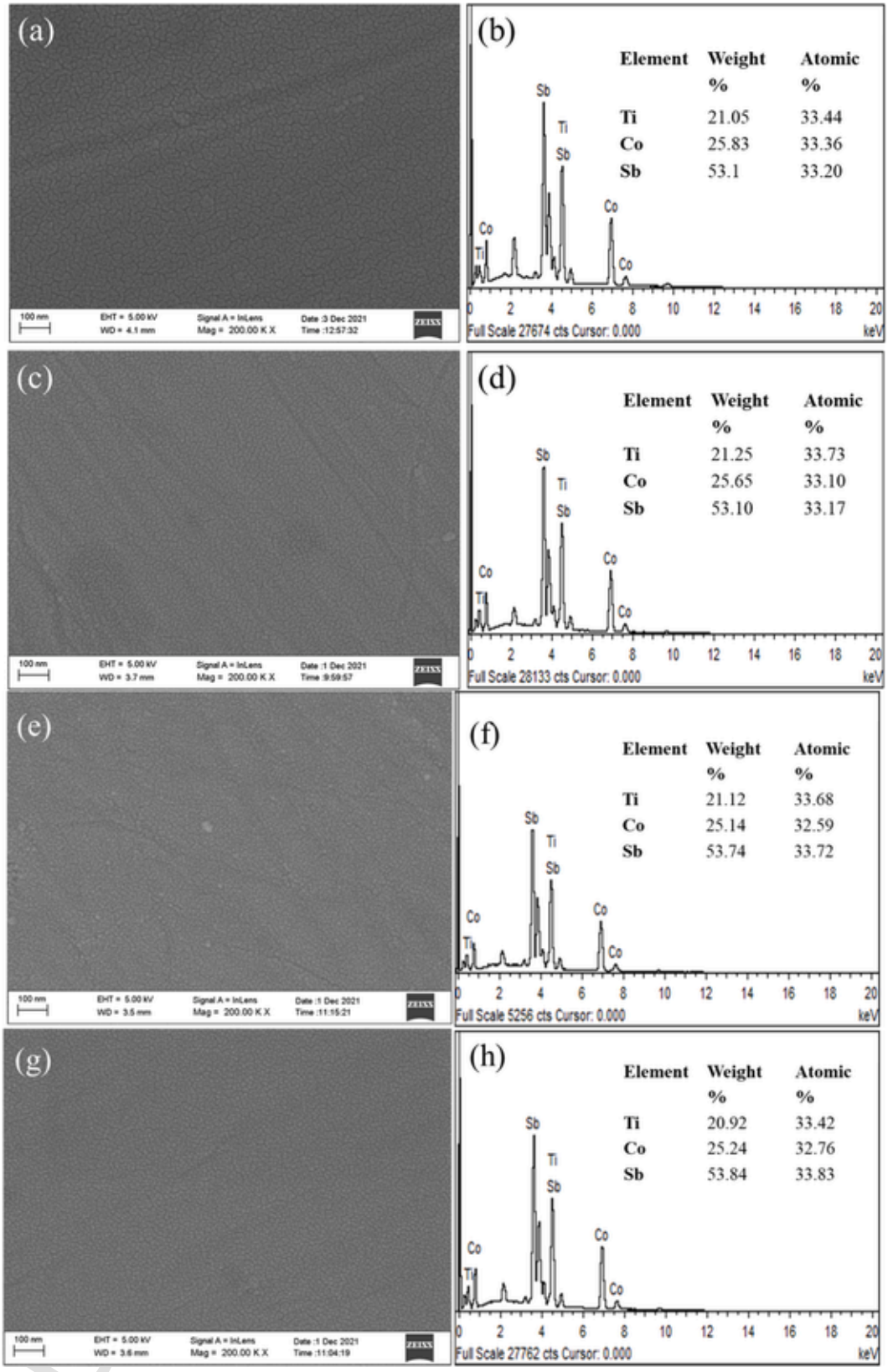

Fig. 3. FESEM images along with EDS analysis of sample S-1 (a–b), S-2 (c–d), S-3 (e–f) and S-4 (g–h).

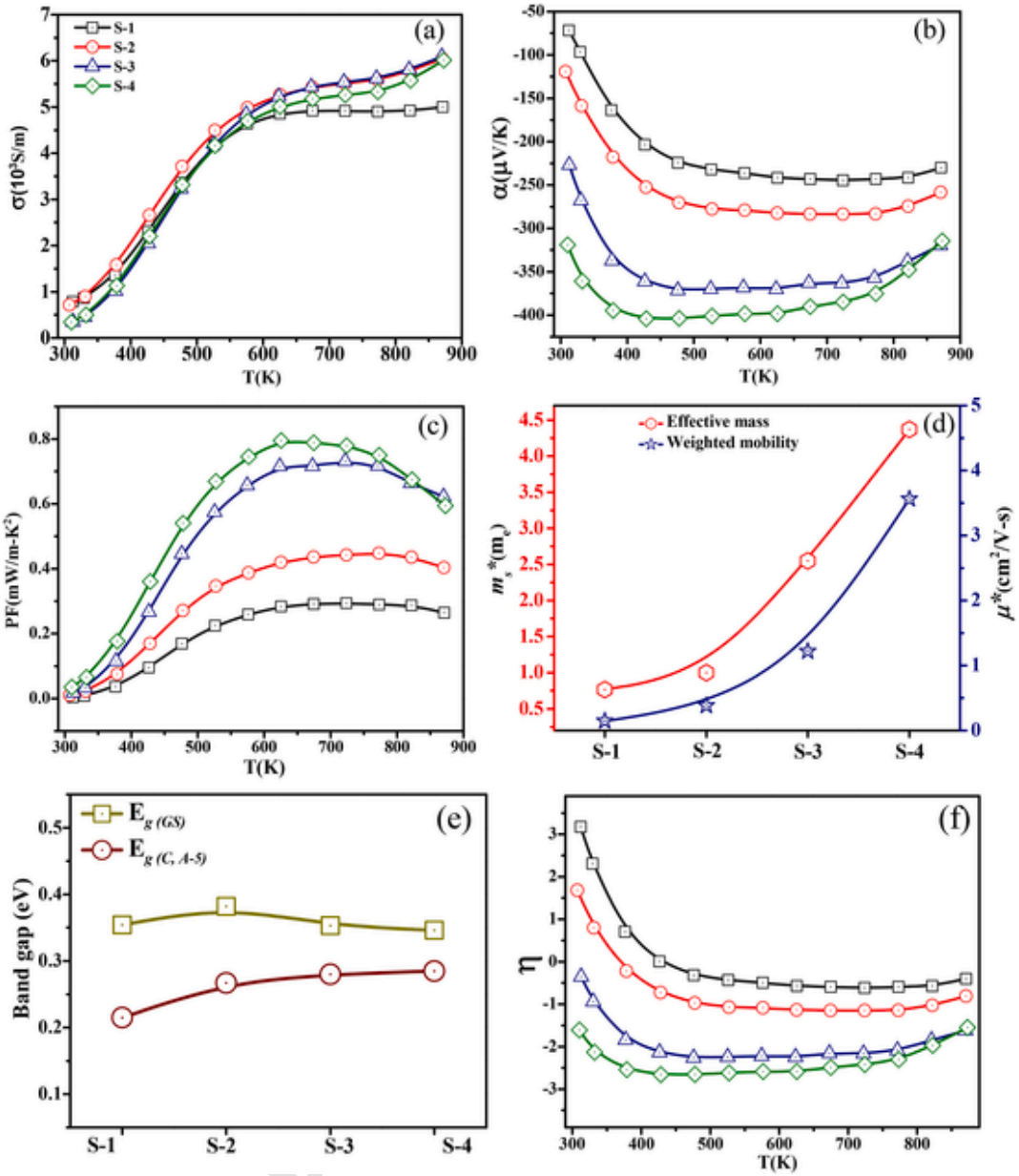

Fig. 4. Temperature dependent electronic properties of all the sample, (a) electrical conductivity, (b) Seebeck coefficient, (c) power factor, (d) effective mass along with weighted mobility, (e) thermal band gap, and (f) reduced chemical potential.

Table 3
Room Temperature Hall data for all TiCoSb samples.

Parameters	S-1	S-2	S-3	S-4
Carrier Density (10^{19} cm^{-3})	10.2	5.79	5.08	3.67
Mobility (cm^2/V-s)	0.22	0.38	0.30	0.39

$$m_S^* \approx \frac{3h^2}{8\pi^2 k_B T}\frac{|\alpha|}{(k_B/e)}\left(\frac{3n}{\pi}\right)^{\frac{2}{3}}$$

Here, e represents electronic charge, h is Planck's constant, and k_B is Boltzmann constant. The calculated room temperature Seebeck effective mass of all the samples is shown in Fig. 4(d). Here, it is observed that m_S^* increases monotonically with increase in the sintering temperature, which is similar to the behavior of α and it is attributed to the combined effect of Seebeck coefficient and carrier concentration. This m_S^* justify electrical conductivity trend at RT which observed in decreasing order and also high effective mass and low carrier concentration are responsible for high PF [45] and same trend we have observed in our data from sample S-1 to S-4. Here it may be noted that the inherent electronic transport properties of TE material are better described by the weighted mobility [12,46] which is calculated, using the relation $\mu^* = \mu\,(m_S^*/m_e)^{3/2}$ at RT, where m_e represents the rest mass of electron. The μ^* is increasing with sintering temperature, which is shown in Fig. 4(d), and thus demonstrate the improvement of inherent electronic transport properties with sintering temperature. Further to investigate, the effect of sintering temperature on band gap tailoring, thermal bandgap $E_{g(GS)}$ of all the samples is estimated from temperature-dependent Seebeck coefficient by using the Goldsmid-Sharp formula [47,48]; $E_{g(GS)} = 2e\alpha_{max}T_{max}$, where α_{max} is the maximum Seebeck coefficient and the temperature corresponding to α_{max} is referred as T_{max}. However, band gap estimated from Goldsmid-Sharp formula shows a small deviation from actual band gap of materials, because Goldsmid-Sharp taken into the account that actual band gap $E_{g(C)} = 10k_BT_{max}$ and it is roughly independent of weighted mobility ratio (A) of majority to

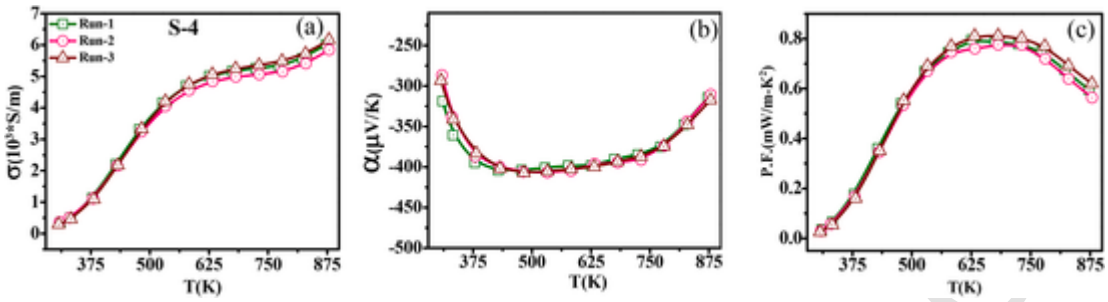

Fig. 5. Repeatability data of electronic transport properties of sample S-4, (a) electrical conductivity, (b) Seebeck coefficient, and (c) power factor.

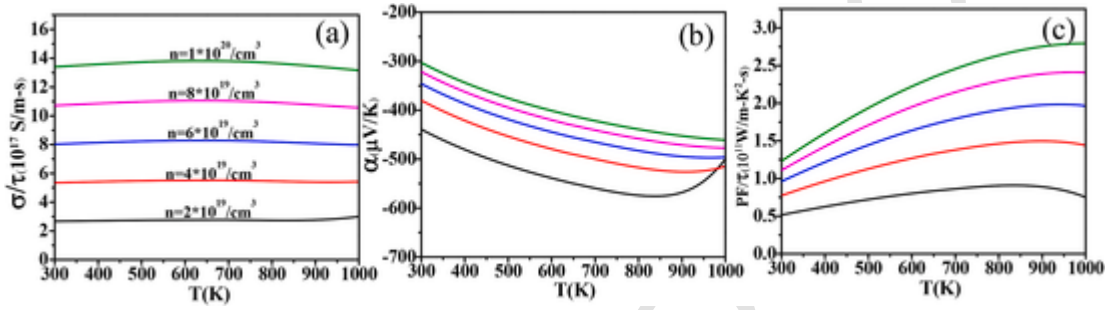

Fig. 6. Theoretical information about thermoelectric electronic transport properties of TiCoSb compound, (a) electrical conductivity, (b) Seebeck coefficient, and (c) power factor.

minority carriers. Therefore, when the band gap is less than $10k_BT_{max}$, it show discrepancy from Goldsmid-Sharp formula, therefore we have also evaluated corrected band gap of our sample by using the relation estimated by Gibbs et al. [48]. Here, we have taken a reasonable value of A = 5 considering the large mobility difference between electrons and holes as most of other intrinsic half Heusler compounds show, because their band gap is less than $5k_BT_{max}$ [48,49]. Both the Goldsmid-Sharp band gap $E_{g(GS)}$ and the corrected band gap $E_{g(C,\ A\text{-}5)}$ of all the samples are shown in Fig. 4(e), where we have observed that the sintering temperature marginally affect to thermal band gap as shown in Fig. 4(e). This thermal band gap is found to be low as compared to the theoretically calculated band gap as illustrated in Fig. 1(b), which can be attributed to the assumptions taken in to account while performing theoretical calculations and synthesis defects [10].

Furthermore to understand the effect of sintering temperature on Fermi level, we have calculated the reduced chemical potential (η) of all the synthesized samples with the assistance of operating temperature-dependent electrical transport properties, using the following parametric equations [44]:

$$\sigma_{E_0} = \sigma.exp\left(\frac{|\alpha|}{k_B/e} - 2\right),$$
$$\sigma = \sigma_{E_0}.\ln(1+e^{\eta})$$

Here, η is related with the position of Fermi level from the conduction band edge [44]. The temperature-reliant η of all the samples is shown in Fig. 4(f). It is clear from Fig. 4(f) that at RT, η is reducing monotonically with sintering temperature, i.e. the Fermi level shifts towards the valence band [44]. Furthermore, η decreases up to a certain temperature and then started increasing which explain the behavior of temperature dependent α of all the samples. To check the thermal stability of the synthesized samples, the electronic transport properties of sample S-4 have been repeated three times as shown in Fig. 5(a–c). The temperature dependent electronic transport properties measured for three temperature cycles overlap to each other, suggesting the thermal stability of the material.

The theoretical temperature dependent electronic transport properties of TiCoSb compound at different electron carrier concentration ranging from 2×1019 to 1×1020 cm-3, are shown in Fig. 6(a–c). As is evident from Fig. 6(a), the magnitude of electrical conductivity at different carrier concentration increases with temperature. Seebeck coefficient of TiCoSb at different carrier concentration is illustrated in Fig. 6 (b), which shows that Seebeck coefficient rises with operating temperature till a finite value after that it achieved saturation or reduces, which is in good agreement with observed trend in experimental data (Fig. 4 (b)). Moreover, the power factor term, illustrated in Fig. 6(c), enhances with increment in temperature and a shoulder like structure is formed, thus, exhibiting consistency with our experimental results. The figure confirms that the peak of power factor shifts toward higher temperature, due to the combined effect of σ/τ and α

In addition to electronic transport properties the mechanical properties of TE materials play an imperative role for the device fabrication. Therefore, in order to see the effect of synthesis parameters on mechanical properties, the micro-hardness and fracture toughness of all the synthesized TiCoSb samples were measured, which are displayed in Fig. 7. The fracture toughness of all samples is obtained using a simple equation of half penny model [50] based on Vickers indentation, $K_c = 0.0752\frac{P}{c^{3/2}}$. Here, K_c represents fracture toughness, P is the load of the indenter and c is the average length of cracks from the center of indentation as schematically shown in Fig. 7(a), c is average of c1, c2, c3, and c4. Fig. 7(b) illustrates that the micro-hardness increases monotonically with sintering temperature, with the value ranging from 7.60 ± 0.42 GPa to 8.58 ± 0.51 GPa. The micro-hardness value obtained for all the samples is comparable to the previously reported results [51]. This marginal increase in micro-hardness values with increase in sintering temperature can be due to the dependency of micro-hardness on the density of samples [51,52]. As sintering temperature increases, the density of samples also increases monotonically as shown in Table 2. The observed values of the micro-hardness is much higher than that of the commercial materials(Bi_2Te_3, PbTe) and is close to values reported for HH alloys [53–55]. The fracture toughness of all the synthesized samples is presented in Fig. 7(b), Here it is observed, the fracture toughness increases with sintering temperature and the observed values are in well agreement to values reported in literature for HH alloys [54] and we have also compared these mechanical properties with some other bulk thermoelectric materials as illustrated in Table 4.

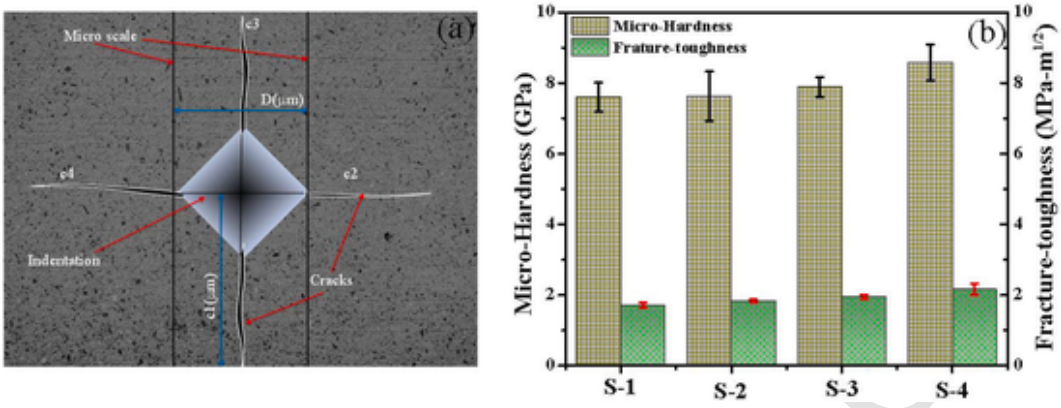

Fig. 7. (a) Schematic diagram of generated cracks in micro indention, (b) Micro-hardness and fracture toughness along with the standard deviation of all the TiCoSb samples.

Table 4
Micro-hardness and fracture-toughness comparison with some other bulk thermoelectric compounds.

Compound	Synthesis route	Micro-hardness (GPa)	Fracture-toughness (MPa-m$^{1/2}$)	References
Bi_2Te_3	SPS	~ 0.63	~ 1.15	[56]
SiGe	Hot Press	12.4–14.7	0.98–1.03	[57]
PbTe	Cast	~ 0.325 - 0.37	–	[55]
LAST(AgPbSbTe)	Furnace Heating	~ 0.52 - 0.93	–	[58]
La_{3-x} Te_4	Hot press	~ 3.28–4.31	~ 0.7	[59]
TiNiSn	Hot press	9.8	–	[51]
ZrNiSn	Hot press	9.9	–	[51]
TiCoSb	Cast	8.1	–	[51]
$Ti_{0.5}Hf_{0.5}Co_{0.5}Ir_{0.5}Sb_{1-x}Sn_x$ (x = 0–0.4)	Ball milling + Hot press	–	2.2–2.6	[54]
TiCoSb, S-4	Arc melting + SPS	~ 8.5	~ 2.1	Present Study

5. Conclusion

In summary, we have synthesized pristine TiCoSb by employing the facile and rapid synthesis route of arc melting followed by SPS. In order to study the effect of synthesis parameters on micro-structural, thermoelectric and mechanical properties, four samples of pristine TiCoSb were sintered at different sintering temperatures 1273 K, 1323 K, 1373 K, and 1423 K, respectively. The structural and micro-structural study confirms that all the synthesized samples are in single HH phase and increased crystallite size is observed with increasing sintering temperature. Further, the observed electronic transport properties at RT suggest that on increasing the sintering temperature, the electrical conductivity marginally decreases, while the Seebeck coefficient significantly increases, resulting enhanced power factor was observed at higher sintering temperatures. The maximum power factor ~0.79 mW/m-K^2 at 625K has been achieved for the sample S-4. In mechanical properties, the results of micro hardness and fracture toughness are better than the most of TE materials, and it was found that the micro-hardness and fracture toughness exhibit an increasing trend with increase in the sintering temperature. Our first principles calculations of electronic structure and transport properties are in agreement with the measured data.

CRediT authorship contribution statement

Ajay Kumar Verma: Methodology, Data curation, Formal analysis, Writing – original draft. **Kishor Kumar Johari:** Methodology, Formal analysis. **Kriti Tyagi:** Writing – review & editing. **S.R. Dhakate:** Writing – review & editing. **Bhasker Gahtori:** Conceptualization, Visualization.

Declaration of competing interest

The authors declare that they have no known competing financial interests or personal relationships that could have appeared to influence the work reported in this paper.

Acknowledgments

The authors are thankful to Director, CSIR-NPL, New Delhi, India for his kind encouragement and support. AKV would like to acknowledge the financial support from UGC-India. DKS thanks to SERB for providing financial support vide letter no. PDF/2020/002789. The technical support given by Mr. Radhey Shyam, and Mr. Naval Kishor Upadhyay are also gratefully acknowledged. KKJ would like to acknowledge the financial support provided by CSIR-India. We acknowledge Council of Scientific and Industrial Research Fourth Paradigm Institute (CSIR-4PI) Bengaluru for providing computational facility. Mr. Abhishek Yadav has checked the plagiarism of manuscript by utilizing the software available in the library of CSIR-NPL, New Delhi.

References

[1] J.-W.G. Bos, R.A. Downie, Half-Heusler thermoelectrics: a complex class of materials, J. Phys. Condens. Matter 26 (2014) 433201.
[2] D.K. Misra, J. Makongo, P. Sahoo, M.R. Shabetai, P. Paudel, K.L. Stokes, P.F. Poudeu, Microstructure and thermoelectric properties of mechanically alloyed Zr0. 5Hf0. 5Ni0. 8Pd0. 2Sn0. 99Sb0. 01/WO3 half-heusler composites, Sci. Adv. Mater. 3 (2011) 607–614.
[3] T. Zhu, C. Fu, H. Xie, Y. Liu, X. Zhao, High efficiency half-Heusler thermoelectric materials for energy harvesting, Adv. Energy Mater. 5 (2015) 1500588.
[4] C. Fu, T. Zhu, Y. Liu, H. Xie, X. Zhao, Band engineering of high performance p-type FeNbSb based half-Heusler thermoelectric materials for figure of merit zT > 1, Energy Environ. Sci. 8 (2015) 216–220.
[5] C. Fu, T. Zhu, Y. Pei, H. Xie, H. Wang, G.J. Snyder, Y. Liu, Y. Liu, X. Zhao, High band degeneracy contributes to high thermoelectric performance in p-type half-Heusler compounds, Adv. Energy Mater. 4 (2014) 1400600.
[6] N.S. Chauhan, S. Bathula, A. Vishwakarma, R. Bhardwaj, B. Gahtori, A.K. Srivastava, M. Saravanan, A. Dhar, A nanocomposite approach for enhancement of thermoelectric performance in Hafnium-free Half-Heuslers, Materialia 1 (2018) 168–174.
[7] R.J. Quinn, J.-W.G. Bos, Advances in half-Heusler alloys for thermoelectric power generation, Materials Advances 2 (2021) 6246–6266.
[8] S.J. Poon, Half Heusler compounds: promising materials for mid-to-high temperature thermoelectric conversion, J. Phys. Appl. Phys. 52 (2019) 493001.
[9] S.J. Poon, Recent advances in thermoelectric performance of half-Heusler

compounds, Metals 8 (2018) 989.
[10] K.K. Johari, R. Bhardwaj, N.S. Chauhan, B. Gahtori, S. Bathula, S. Auluck, S. Dhakate, Band structure modification and mass fluctuation effects of isoelectronic germanium-doping on thermoelectric properties of ZrNiSn, ACS Appl. Energy Mater. 3 (2019) 1349–1357.
[11] N.S. Chauhan, S. Bathula, A. Vishwakarma, R. Bhardwaj, K.K. Johari, B. Gahtori, M. Saravanan, A. Dhar, Compositional tuning of ZrNiSn half-Heusler alloys: thermoelectric characteristics and performance analysis, J. Phys. Chem. Solid. 123 (2018) 105–112.
[12] K.K. Johari, R. Bhardwaj, N.S. Chauhan, S. Bathula, S. Auluck, S. Dhakate, B. Gahtori, High thermoelectric performance in n-type degenerate ZrNiSn-based half-heusler alloys driven by enhanced weighted mobility and lattice anharmonicity, ACS Appl. Energy Mater. 4 (2021) 3393–3403.
[13] H. Xie, H. Wang, C. Fu, Y. Liu, G.J. Snyder, X. Zhao, T. Zhu, The intrinsic disorder related alloy scattering in ZrNiSn half-Heusler thermoelectric materials, Sci. Rep. 4 (2014) 6888.
[14] N.S. Chauhan, S. Bathula, A. Vishwakarma, R. Bhardwaj, B. Gahtori, A. Kumar, A. Dhar, Vanadium-doping-induced resonant energy levels for the enhancement of thermoelectric performance in Hf-free ZrNiSn half-Heusler alloys, ACS Appl. Energy Mater. 1 (2018) 757–764.
[15] N.S. Chauhan, S. Bathula, B. Gahtori, S.D. Mahanti, A. Bhattacharya, A. Vishwakarma, R. Bhardwaj, V.N. Singh, A. Dhar, Compositional tailoring for realizing high thermoelectric performance in hafnium-free n-type ZrNiSn half-heusler alloys, ACS Appl. Mater. Interfaces 11 (2019) 47830–47836.
[16] X. Yang, Z. Jiang, H. Kang, Z. Chen, E. Guo, D. Liu, F. Yang, R. Li, X. Jiang, T. Wang, Enhanced thermoelectric performance of Zr1−x Ta x NiSn half-heusler alloys by diagonal-rule doping, ACS Appl. Mater. Interfaces 12 (2019) 3773–3783.
[17] L. Wang, L. Miao, Z. Wang, W. Wei, R. Xiong, H. Liu, J. Shi, X. Tang, Thermoelectric performance of half-Heusler compounds TiNiSn and TiCoSb, J. Appl. Phys. 105 (2009) 013709.
[18] H. Joshi, D. Rai, A. Laref, R. Thapa, Electronic, and thermoelectric properties of half-heusler compounds MCoSb (M= Ti, Zr, Hf): a first principles study, Mater. Res. Express 6 (2019) 066307.
[19] D. Zou, S. Xie, Y. Liu, J. Lin, J. Li, Electronic structure and thermoelectric properties of half-Heusler Zr0. 5Hf0. 5NiSn by first-principles calculations, J. Appl. Phys. 113 (2013) 193705.
[20] A.N. Gandi, U. Schwingenschlögl, Electron dominated thermoelectric response in MNiSn (M: Ti, Zr, Hf) half-Heusler alloys, Phys. Chem. Chem. Phys. 18 (2016) 14017–14022.
[21] B. Xu, J. Zhang, X.-F. Li, G.-Q. Yu, S.-S. Ma, Y.-S. Wang, L. Yi, Electronic structure and assessment of thermoelectric performance of TiCoSb, Mater. Res. Innovat. 18 (2014) 104–107.
[22] T. Wu, W. Jiang, X. Li, S. Bai, S. Liufu, L. Chen, Effects of Ge doping on the thermoelectric properties of TiCoSb-based p-type half-Heusler compounds, J. Alloys Compd. 467 (2009) 590–594.
[23] T. Wu, W. Jiang, X. Li, Y. Zhou, L. Chen, Thermoelectric properties of p-type Fe-doped TiCoSb half-Heusler compounds, J. Appl. Phys. 102 (2007) 103705.
[24] M. Zhou, C. Feng, L. Chen, X. Huang, Effects of partial substitution of Co by Ni on the high-temperature thermoelectric properties of TiCoSb-based half-Heusler compounds, J. Alloys Compd. 391 (2005) 194–197.
[25] T. Sekimoto, K. Kurosaki, H. Muta, S. Yamanaka, Thermoelectric properties of Sn-doped TiCoSb half-Heusler compounds, J. Alloys Compd. 407 (2006) 326–329.
[26] P. Qiu, X. Huang, X. Chen, L. Chen, Enhanced thermoelectric performance by the combination of alloying and doping in TiCoSb-based half-Heusler compounds, J. Appl. Phys. 106 (2009) 103703.
[27] M. Zhou, L. Chen, C. Feng, D. Wang, J.-F. Li, Moderate-temperature thermoelectric properties of TiCoSb-based half-Heusler compounds Ti 1− x Ta x Co Sb, J. Appl. Phys. 101 (2007) 113714.
[28] G.K. Madsen, D.J. Singh, BoltzTraP. A code for calculating band-structure dependent quantities, Comput. Phys. Commun. 175 (2006) 67–71.
[29] G. Kresse, J. Furthmüller, Efficient iterative schemes for ab initio total-energy calculations using a plane-wave basis set, Phys. Rev. B 54 (1996) 11169.
[30] G. Kresse, J. Furthmüller, Efficiency of ab-initio total energy calculations for metals and semiconductors using a plane-wave basis set, Comput. Mater. Sci. 6 (1996) 15–50.
[31] J. Heyd, G.E. Scuseria, M. Ernzerhof, Hybrid functionals based on a screened Coulomb potential, J. Chem. Phys. 118 (2003) 8207–8215.
[32] J. Toboła, J. Pierre, Electronic phase diagram of the XTZ (X= Fe, Co, Ni; T= Ti, V, Zr, Nb, Mn; Z= Sn, Sb) semi-Heusler compounds, J. Alloys Compd. 296 (2000) 243–252.
[33] J. Tobola, J. Pierre, S. Kaprzyk, R. Skolozdra, M. Kouacou, Crossover from semiconductor to magnetic metal in semi-Heusler phases as a function of valence electron concentration, J. Phys. Condens. Matter 10 (1998) 1013.
[34] V. Mote, Y. Purushotham, B. Dole, Williamson-Hall analysis in estimation of lattice strain in nanometer-sized ZnO particles, J.Theor.Appl. Phys. 6 (2012) 6.
[35] L.K. Singh, A. Bhadauria, S. Jana, T. Laha, Effect of sintering temperature and heating rate on crystallite size, densification behaviour and mechanical properties of Al-MWCNT nanocomposite consolidated via spark plasma sintering, Acta Metall. Sin. 31 (2018) 1019–1030.
[36] S.B. Waje, M. Hashim, I. Ismail, Effects of sintering temperature on grain growth and the complex permeability of Co0. 2Ni0. 3Zn0. 5Fe2O4 material prepared using mechanically alloyed nanoparticles, J. Magn. Magn Mater. 323 (2011) 1433–1439.
[37] C.S. Birkel, W.G. Zeier, J.E. Douglas, B.R. Lettiere, C.E. Mills, G. Seward, A. Birkel, M.L. Snedaker, Y. Zhang, G.J. Snyder, Rapid microwave preparation of thermoelectric TiNiSn and TiCoSb half-Heusler compounds, Chem. Mater. 24 (2012) 2558–2565.
[38] A. Vishwakarma, N.S. Chauhan, R. Bhardwaj, K.K. Johari, S.R. Dhakate, B. Gahtori, S. Bathula, Compositional modulation is driven by aliovalent doping in n-type TiCoSb based half-Heuslers for tuning thermoelectric transport, Intermetallics 125 (2020) 106914.
[39] C.-H. Lee, P. Dharmaiah, J.-W. Song, K.-Y. Jeong, S.-J. Hong, Influence of Spark Plasma Sintering Temperature on Microstructure and Tthermoelectric Properties of Cu-Doped Bi0. 5Sb1. 495Te3 Compound, vol. 65, Archives of Metallurgy and Materials, 2020.
[40] Y. Gelbstein, N. Tal, A. Yarmek, Y. Rosenberg, M.P. Dariel, S. Ouardi, B. Balke, C. Felser, M. Köhne, Thermoelectric properties of spark plasma sintered composites based on TiNiSn half-Heusler alloys, J. Mater. Res. 26 (2011) 1919–1924.
[41] L. Chen, S. Gao, X. Zeng, A. Mehdizadeh Dehkordi, T. Tritt, S. Poon, Uncovering high thermoelectric figure of merit in (Hf, Zr) NiSn half-Heusler alloys, Appl. Phys. Lett. 107 (2015) 041902.
[42] K.-y. Jeong, C.H. Lee, P. Dharmaiah, S.-J. Hong, Optimization of spark plasma sintering temperature conditions for enhancement of thermoelectric performance in gas-atomized Bi 0.5 Sb 1.5 Te 3 compound, J. Kor. Powder Metall. Inst. 24 (2017) 108–114.
[43] Y.-H. Lee, T. Koyanagi, Thermoelectric properties of n-Bi-Sb sintered alloys prepared by spark plasma sintering method, in: Proceedings ICT2001. 20 International Conference on Thermoelectrics (Cat. No. 01TH8589), IEEE, 2001, pp. 278–281.
[44] A. Zevalkink, D.M. Smiadak, J.L. Blackburn, A.J. Ferguson, M.L. Chabinyc, O. Delaire, J. Wang, K. Kovnir, J. Martin, L.T. Schelhas, A practical field guide to thermoelectrics: fundamentals, synthesis, and characterization, Appl. Phys. Rev. 5 (2018) 021303.
[45] G. Xing, J. Sun, Y. Li, X. Fan, W. Zheng, D.J. Singh, Electronic fitness function for screening semiconductors as thermoelectric materials, Physical Review Materials 1 (2017) 065405.
[46] G.J. Snyder, A.H. Snyder, M. Wood, R. Gurunathan, B.H. Snyder, C. Niu, Weighted mobility, Adv. Mater. 32 (2020) 2001537.
[47] H. Goldsmid, J. Sharp, Estimation of the thermal band gap of a semiconductor from Seebeck measurements, J. Electron. Mater. 28 (1999) 869–872.
[48] Z.M. Gibbs, H.-S. Kim, H. Wang, G.J. Snyder, Band gap estimation from temperature dependent Seebeck measurement—deviations from the 2e| S| maxTmax relation, Appl. Phys. Lett. 106 (2015) 022112.
[49] J. Schmitt, Z.M. Gibbs, G.J. Snyder, C. Felser, Resolving the true band gap of ZrNiSn half-Heusler thermoelectric materials, Materials Horizons 2 (2015) 68–75.
[50] A. Moradkhani, H. Baharvandi, M. Tajdari, H. Latifi, J. Martikainen, Determination of fracture toughness using the area of micro-crack tracks left in brittle materials by Vickers indentation test, J. Adv. Ceram. 2 (2013) 87–102.
[51] G. Rogl, A. Grytsiv, M. Gürth, A. Tavassoli, C. Ebner, A. Wünschek, S. Puchegger, V. Soprunyuk, W. Schranz, E. Bauer, Mechanical properties of half-Heusler alloys, Acta Mater. 107 (2016) 178–195.
[52] J. Luo, R. Stevens, Porosity-dependence of elastic moduli and hardness of 3Y-TZP ceramics, Ceram. Int. 25 (1999) 281–286.
[53] R. He, S. Gahlawat, C. Guo, S. Chen, T. Dahal, H. Zhang, W. Liu, Q. Zhang, E. Chere, K. White, Studies on mechanical properties of thermoelectric materials by nanoindentation, physica status solidi (a) 212 (2015) 2191–2195.
[54] C.J. O'Connor, Nanostructured Composite Materials for High Temperature Thermoelectric Energy Conversion, NEW ORLEANS UNIV LA, 2012.
[55] A. Schmitz, J. de Boor, K. Mull, E. Müller, Tailoring the mechanical properties of thermoelectric lead telluride by alloying with non-doping calcium, J. Mater. Sci. 51 (2016) 6933–6943.
[56] L.-D. Zhao, B.-P. Zhang, J.-F. Li, M. Zhou, W.-S. Liu, J. Liu, Thermoelectric and mechanical properties of nano-SiC-dispersed Bi2Te3 fabricated by mechanical alloying and spark plasma sintering, J. Alloys Compd. 455 (2008) 259–264.
[57] A. Kallel, G. Roux, C. Martin, Thermoelectric and mechanical properties of a hot pressed nanostructured n-type Si80Ge20 alloy, Mater. Sci. Eng., A 564 (2013) 65–70.
[58] F. Ren, E. Case, E. Timm, H. Schock, Hardness as a function of composition for n-type LAST thermoelectric material, J. Alloys Compd. 455 (2008) 340–345.
[59] J.M. Ma, S.A. Firdosy, R.B. Kaner, J.-P. Fleurial, V.A. Ravi, Hardness and fracture toughness of thermoelectric La 3− x Te 4, J. Mater. Sci. 49 (2014) 1150–1156.